Incorporation of MnO$_2$ into Egg Yolk Derived P, N, O-Tridoped Carbon for Supercapacitors with Excellent Cycling Stability

Cheng Feng, Dimei Chen[*], Yu Tang, Suqin Chen,Yiyan Liu, Chaoqun Zhu, Weining Xie, Limin Ye, Qingcheng Zhang, Pengcheng Qian, Xin Feng, Xiaomei Dong, Huile Jin[*]

College of Chemistry and Materials Engineering, Institute of New Materials and Industrial Technologies, Wenzhou University, Wenzhou, Zhejiang 325035, China
[*]E-mail: cdm8203@163.com, Huilejin@wzu.edu.cn

The design of novel electrode materials is still challenging in the development of high-performance supercapacitors. To tackle such difficulties, a potentially feasible strategy is recently emerged via the incorporation of pseudocapacitive transition metals into biomass-derived carbon electrodes, in which pseudo-capacity mainly derived from transition metals is efficiently stabilized by the heteroatom doped carbon hosts. In this work, a MnO$_2$-decorated P, N, O-tridoped porous carbon electrode has been developed via a simple hydrothermal reaction by mixing KMnO$_4$ with biomass egg yolk under mild conditions. The as-obtained MnPNC (MnO$_2$ decorated P, N, O-tridoped Porous Carbon) is composed of MnO$_2$ nanosheets wrapped by porous carbon, exhibiting a high specific capacitance of 341 F/g at a current density of 1 A/g in 6 M KOH and an outstanding long-term cycling stability of 15000 cycles. These results indicate that the carbon protecting layer is able to promote the stability of MnO$_2$ during charging/discharging processes.

1. INTRODUCTION

Nowadays, ever-growing energy demands and rapid depletion of fossil fuels is urgently calling for a green, sustainable, high-efficiency and low-cost energy storage technology [1–6]. Supercapacitors, offering a high power density, ultra-long cycle life and excellent safety properties, have been widely applied in energy storage and portable electronic devices [7]. The high-performance supercapacitors are commonly derived from their high surface area, excellent electrical conductivity, good thermal conductivity and porosity of the electrode material [8]. For instance, carbon-based nanomaterials are well known as the most ideal electrode candidates for electric double-layer capacitors because of their

high specific surface area and porous structure [9,10]. However, the low energy density and slow charge/discharge performance are major drawbacks hindering the widespread application of carbon-based supercapacitors [11–13]. Therefore, to fulfill the energy demand in high energy density devices, the capacitance of carbon materials have to be boosted further. Moreover, most carbon materials are derived from non-renewable petroleum-based chemical products [14], which generate a high cost because of the fossil fuel and environmental crisis looming in the near future.

Compared to the conventional pure carbon electrode materials only supporting electric double-layer capacitance, many newly-established heteroatom doped carbon offers extra pseudocapacitance, but transition metals have been demonstrated to contribute much more pseudocapacitance in supercapacitors, due to their larger theoretical capacitance and working potential [15]. To be more specific, manganese dioxide (MnO_2) is referred to as the most promising pseudo-capacitive material because of its high theoretical electrochemical capacitance (1370 F/g), wide output voltage, low cost and environmental friendliness [16]. However, its poor electrical conductivity (10^{-5}-10^{-6} S/cm) and stability [17] still remains a challenge in commercialized MnO_2-based supercapacitors. One effective method is to incorporate MnO_2 into certain conductive frameworks to form hybrid composites [18-20], such as graphene [21,22], graphene oxide [23-25], carbon nanotubes [26,27], which are quite suitable for providing stable scaffolds for MnO_2 and thus improving charge transportation. To date, although many studies have shown the superior electrochemical performance which is relied on the nano-composited MnO_2/carbon structures [28], their poor cycling stability is still a big concern due to the fast deterioration of transition metals.

Recently, our studies revealed that biomass derived carbon materials such as waxberry [29] and egg yolk [30] can significantly enhance both electrochemical performance and cycling stability. The utilization reversible redox reactions/fast Faradaic reactions in transition metals will give rise to a significant enhancement of capacitance. We found the major contribution to the capacitance is from the incorporation of pseudocapacitive transition metal species rather than the heteroatom dopants from biomass materials [31]. Meanwhile, in the biomass-derived heteroatoms-doped carbon materials, the rich heteroatoms could benefit to the electrochemical properties, for example, providing extra pseudocapacitive contributions from the fast faradic reactions between the heteroatom containing functional groups and the electrolyte ions, and in some cases the heteroatoms doping enables the optimization of surface wettability and electronic conductivity [32], both of which are contributing to the improvement of electrochemical performance. More importantly, the carbon layers function as the protecting layer to avoid the dissolution of transition metals into electrolytes, resulting in improved cycling stability.

In this work, we prepared a low-cost and high-performance hybrid MnO_2-decorated P, N, O-triped porous carbon for supercapacitors via a hydrothermal reaction between biomass egg yolk and $KMnO_4$ under mild conditions. The as-prepared MnPNC electrode not only exhibits a high capacitance of 341 F/g at a current density of 1 A/g in 6 M KOH, but also possesses a significantly improved cycling stability of 15000 cycles.

2. EXPERIMENTAL

2.1. Materals

Eggs were purchased from local supermarket, egg yolks were separately collected and dried at 120 °C for use. $KMnO_4$ was obtained from Wuxi Jani Chemical Industry Co., Ltd. Other reagents were analytical grade and used without any further purification. Deionized water was utilized throughout the experiments.

2.2. Preparation of the egg yolks derived MnPNC and PNC composites

474 mg of $KMnO_4$ was mixed with 30 mL deionized water to obtain 0.1 M $KMnO_4$ solution. Subsequently, 9.6 g of dried egg yolks powder was added into the solution and ultrasonicated for 0.5 h. Then, the mixed solution was transferred into a 50 mL teflonlined stainless steel pressure vessel and maintained at 180 °C for 12 h. After the reaction was completed, the mixture was naturally cooling down to room temperature, and the black grease was obtained by three times cleaning and centrifugal separation. The black grease was fully dried at 120 °C for 12 h to obtain crude product. The yielded crude product was then annealed at 1000 °C for 2 h under nitrogen gas protection, the MnPNC composites were finally obtained. PNC (P, N, O-tridoped porous carbon) production was followed by the same procedure for the synthesis of MnPNC without the addition of $KMnO_4$.

2.3. Instruments and characterization

The surface morphologies of the MnPNC composite material were analyzed by the field emission scanning electron microscopy (SEM, FEI-Nova Nanosem 200) images. The transmission electron microscopy (TEM) images were obtained on a JEOL-2010 transmission electron microscope at an acceleration voltage of 200 kV. Energy dispersive X-ray spectroscopy was taken at the same time as TEM measurement. The crystallographic structures of the as-synthesized samples were analyzed with a powder X-ray diffraction (XRD, Bruker D8 Advance, Cu Kα radiation, $\lambda = 0.15406$ nm) system. Raman spectroscopy was performed using JY-T643200 from France at ambient temperature with a laser excitation of 514 nm. Moreover, the compositions were further measured by X-ray photoelectron spectroscopy (XPS, Kratos Axis Ultradld) , using Mono Al Kαradiationat a power of 120 W (8 mA, 15 kV). Percentage(s) of various elements and functional groups were calculated on the basis of peak areas from the deconvoluted XPS spectra. Multi-point N_2 adsorption-desorption experiment was performed on an automatic Micromeritics ASAP 2020 analyzer at 77 K. The sample was degassed at 300 °C for 6 h in vacuum before adsorption measurement. The specifc surface area was calculated using the BET equation. The pore-size distribution was calculated from the isotherm adsorption branches based on the Barrett-Joyner-Halenda (BJH) model.

2.4. Electrochemical measurements

To fabricate working electrodes, MnPNC active materials, acetylene black, and polytetrafluroethylene (PTFE, 5 wt%) were mixed in a mortar at a mass ratio of MnPNC : PTFE :

acetylene black of 8:1:1. The mixture was then spread on a nickel foam, followed by the drying at 120 °C for 1h.

The as-prepared electrodes were pressed under a pressure of 10 MPa. The mass loading of the active materials on Ni form was set to approximately 1.5–2.5 mg/cm^2. All of the electrochemical measurements were carried out at room temperature (25 °C) by using a traditional three-electrode system in 6 M KOH aqueous electrolyte. Pt wire was applied as a counter electrode, and the potentials were measured with respect to standard calomel reference electrode (SCE). Cyclic voltammetry (CV) and galvanostatic charge/discharge (GCD) performance were carried out by using CHI760D electrochemical workstation at room temperature. Electrochemical impedance measurements (EIS) were conducted in the 100 kHz to 0.01 Hz at open circuit voltage. The gravimetric capacitance of a working electrode can be calculated from the charge–discharge and CV plots based on the following Equations :

$$C_s (\mathrm{F/g}) = \frac{2I \times \Delta t}{m \times \Delta V}$$

where Cs (F/g) is the gravimetric capacitance of the single electrode, I (A) is the current value of CV curves, Δt (s) is the discharge time, ΔV is the width of the discharging potential, and m (g) is the loading on each electrode active materials. Moreover, the energy density (Wh/kg) and the maximum power density (W/kg) of as-fabricated devices were calculated from the GCD curves according to Eqs. respectively.

$$E(\mathrm{Wh/kg}) = \frac{0.5\,C_T \times \Delta V^2}{3.6}$$

$$P(\mathrm{W/kg}) = \frac{E \times 3600}{\Delta t}$$

Where E (W h/kg) is the energy density, P (W/kg) is the power density, Cs (F/g) is the specific capacitance, ΔV (V) is the potential window of device, and Δt (s) is the discharge time.

3. RESULTS AND DISCUSSION

The scanning electron microscope (SEM) image in Fig. 1 shows an irregular cluster morphology of as-prepared PNC. However, MnPNC was calcined as a nanosheet rather than cluster, indicating Mn-based compounds effectively build the nanosheet scaffolds that are decorated by P, N, O-tridoped porous carbon on the Mn-derived nanosheet surface. Fig. 2b and 2c further illustrate an amphorous carbon layer is covered on the surface of nanosheet structured MnO$_2$ where the crystalline phase is confirmed as (002) facet of MnO$_2$, with an interplanar distance of 0.22 nm. Moreover, high-angle annular dark-field scanning transmission electron microscopy (HAADF-STEM) was carried out to examine more details about the possible elements existed in MnPNC. As it can be seen in Fig. 2d-2i, the outside carbon layer is mostly composed of nitrogen (N), phosphor (P) and oxygen (O), suggesting the formation of PNC. It is worth to note that all the elements are well dispersed among the MnPNC samples.
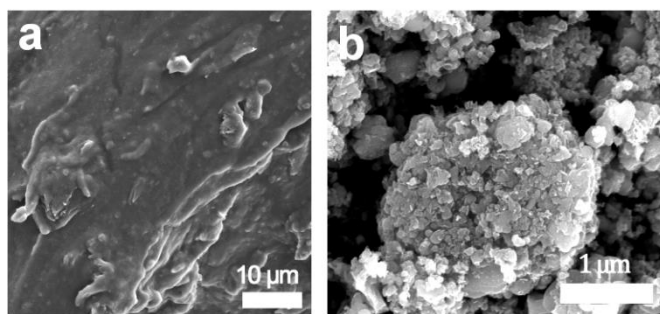
Figure 1. SEM images of (a) PNC after hydrothermal reaction and (b) PNC after calcination.
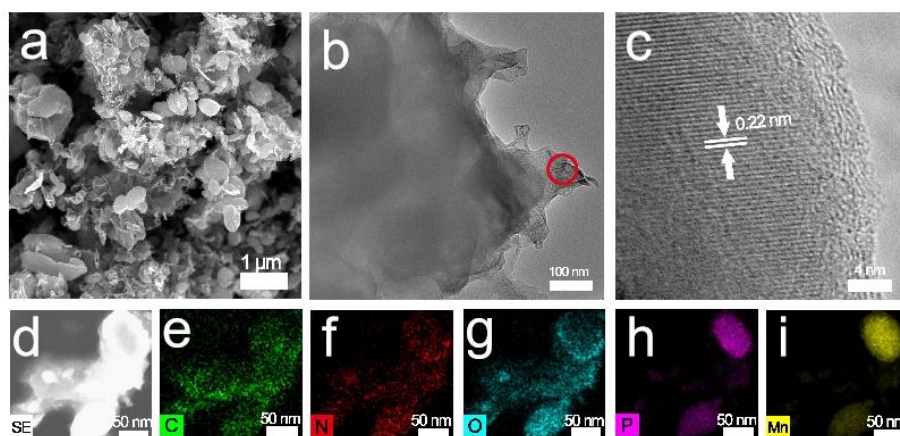
Figure 2. (a) SEM images of MnPNC, (b) and (c) TEM image of MnPNC, (d) element mapping images of MnPNC: (e) C, (f) N, (g) O, (h) P, (i) Mn.

According to the Brunauer-Emmett-Teller (BET) measurement in Fig. 3a, the specific surface area of MnPNC (127.37 m^2/g) is surprisingly larger than PNC (26.70 m^2/g). The probable reason is the occurance of gas evolution during the reaction between KMnO$_4$ and egg yolk, which will subsequently give rise to massive production of nanoporous configuration, thus leading to the improved electrolyte migration and enhanced electrochemical kinetics. Raman spectra in Fig. 3b also demonstrated the existence of abundant defects. The intensity ratio of D and G bands (I_D/I_G) in Raman spectra for the MnPNC and PNC is 0.98 and 1, respectively, suggesting that heteroatom (P, N, O) doping induced rich defects are fascinating and aid in the promotion of electrochemical performance.

The detailed chemical states of heteroatom dopants were further investigated by X-ray photoelectron spectroscopy (XPS) in Fig. 3c. Compared to PNC, the atomic ratio of oxygen is greatly elevated when Mn species was incorporated. What's more, Mn 2p peak is composed of Mn 2p$_{1/2}$ and Mn 2p$_{3/2}$ located at 654.48 and 642.53 eV, respectively. The spin-energy separation of 11.95 eV suggests the formation of MnO$_2$ in MnPNC. However, X-ray diffraction (XRD) pattern of MnPNC in Fig. 3d only partially confirms the TEM and XPS results, in which diffraction peaks can be indexed not only to the MnO$_2$ (JCPDS NO.12-0141), but also to Mn$_2$P (JCPDS NO.65-3545).
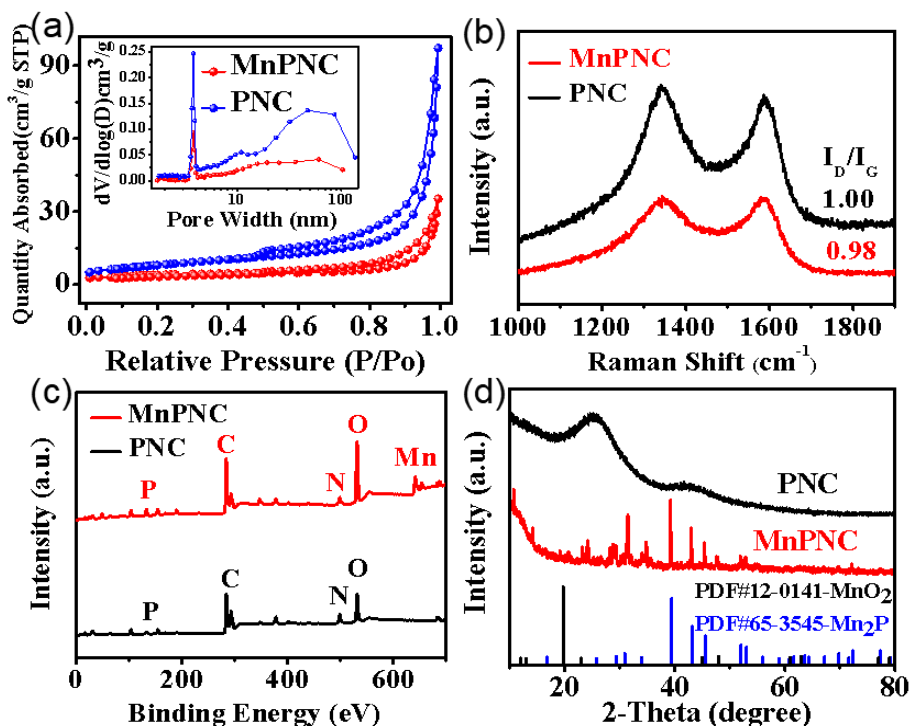
Figure 3. (a) N$_2$ adsorption–desorption curves and pore size distribution of MnPNC and PNC, (b) Raman spectra of the MnPNC and PNC, (c) XPS spectra of the MnPNC and PNC, (d) XRD patterns of MnPNC and PNC.
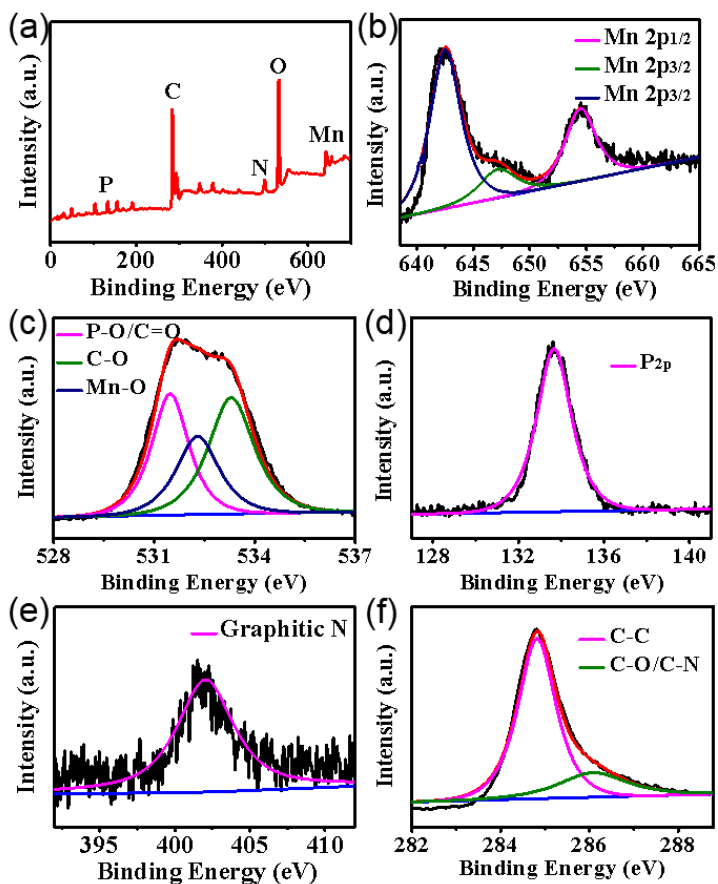
Figure 4. (a) XPS spectra of the MnPNC, (b) Mn 2p, (c) O 1s, (d) P 2p, (e) N 1s, (f) C 1s.

Considering the rare P at% in MnPNC (approximately 0.6 at% in Fig. 4d), Mn_2P is recognized as a minor component in Mn-based active materials. Due to the failure of searching the facets of Mn_2P in transmission electron microscopy (TEM), It can be concluded that minor Mn_2P phase is buried inside MnPNC samples and phosphorus elements are mostly contributed to the dopants on carbon. As the atomic ratio between N and P is unchanged in Fig. 4 and Fig. 5, only oxygen is occupied more in MnPNC in Fig. 4c which is able to form MnO_2 phase.
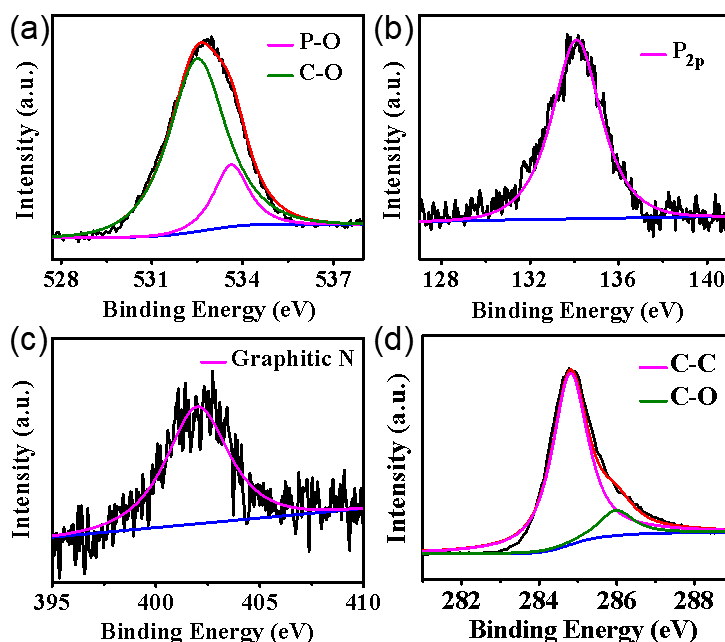
Figure 5. XPS spectra of the PNC, (a) O 1s, (b) P 2p, (c) N 1s, (d) C 1s.

Electrochemical properties of MnPNC were then evaluated by CV, GCD and EIS in 6 M KOH electrolyte. It can be found that the pseudocapacitance is neatly zero in case of PNC in Fig. 6a and 6b. However, MnPNC electrode exhibits a unconventionally high capacitance of 341 F/g at 1 A/g. These results clearly demonstrate the capacitance is mostly derived from the incorporation of transition metal MnO_2 rather than the heteroatom dopants from biomass. Meanwhile, the as-prepared MnPNC composites possessed relatively higher surface area than PNC also offers numerous accessible electroactive sites for electrochemical reactions which guarantee the fast electrolyte ions transport.

Generally, the incorporation of transition metals into carbon matrix will deteriorate charge transfer resistance. In order to examine the role of MnO_2 in Nyquist plots, electrochemical impedance spectrum (EIS) measurements were conducted in a three-electrode cell system in 6 M KOH. The Nyquist plots of MnPNC and PNC behaved quite similar in Fig. 6d with a relatively low equivalent series resistance of ~2 ohms. Both Nyquist plot shows a semicircle in the high–middle frequency region and a straight line arising in low frequency region. It is worth noting the presence of MnO_2 will sacrifice some supercapacitive property due to the poorly sloped straight line in the low-frequency region. Nevertheless,

the introduction of transition metal won't lead to a tremendous decrease of resistance, which is mainly attributed from the protecting layer efficiently prevents the dissolution of transition metals into electrolytes, and also provides a rapid charge transfer pathway. Such unique configuration of MnPNC delivers a high energy density of 38.4 Wh/kg (Fig. 6e) at the power density of 0.2 W/kg in an alkaline electrolyte, and maintains an outstandingly high cycling stability of 15000 cycles at 1 mV/s (Fig. 6f).

As is well known, the carbonization temperature has a significant impact on the supercapacitive performance of MnPNC, hence in this work, we have actually optimized our carbonization temperatures in which 1000 °C exhibits the best charge storage performance. As shown in Fig. 7d, 1000 °C calcination results in pronounced redox peaks and excellent supercapacitive performance.
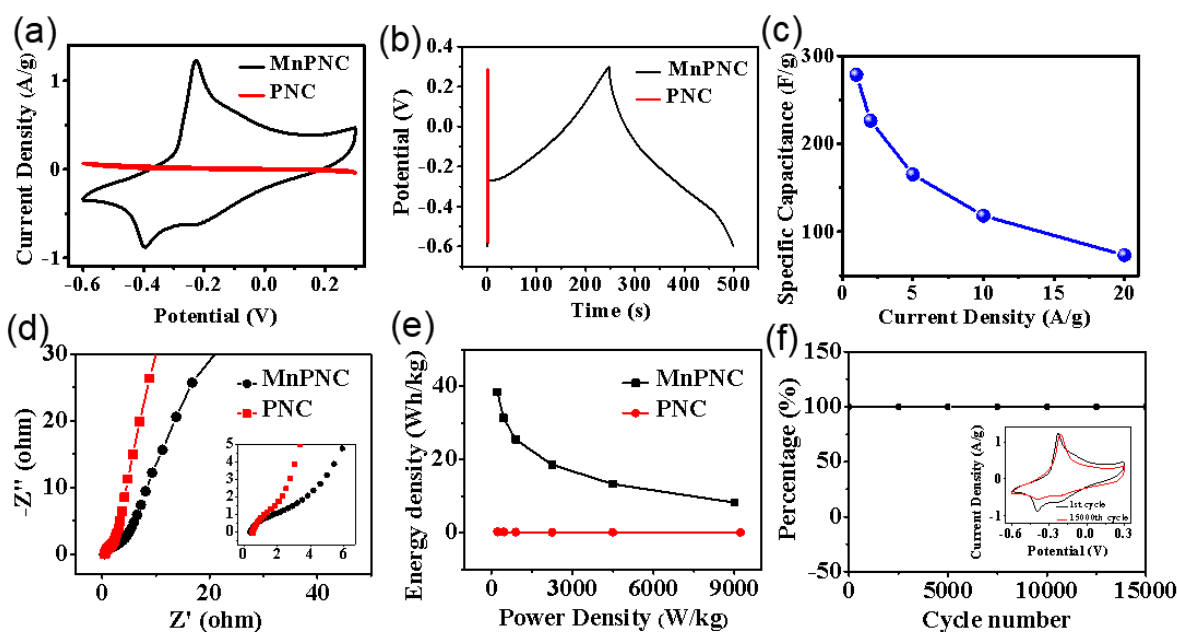
Figure 6. Electrochemical performance in 6 M KOH electrolyte. (a) CV curves of MnPNC and PNC at a scan rate of 1 mV/s, (b) Galvanostatic charging/discharging curves of MnPNC and PNC at 1 A/g, (c) Rate capability of MnPNC, (d) Electrochemical impedance spectrum (EIS) obtained from MnPNC and PNC, (e) Ragone plot of MnPNC and PNC, (f) The cycling performance of MnPNC after 15000 CV tests.

Compared with the electrochemical performance of carbon/MnO_2 based supercapacitors reported in litherature (Table 1), our MnPNC electrode exhibits the best cycling stability among all the existing MnO_2-based materials although our specific capacitance is not that attractive. In general, there is a trade-off relationship between the incorporation contents of transition metals and electrochemical performance [31]. When the mass loading of MnO_2 is low, such as 12.9 wt% [34], ~20 wt% [36], 29.7 wt% [40], 40 wt% [51], the resulted pseudocapacitance all exhibits low values due to the lack of enough loading of active materials. When the mass loading of MnO_2 is beyond certain criteria such as 50 wt% of MnO_2 in MnO_2@C-100 [44], 115.9 wt% of MnO_2 in MnO_2/HCS-30 [45], 260 wt% of MnO_2 in

CNT@NCT@MnO_2 [47], 80 wt% of MnO_2 in MnO_2/N-C [52], more active transition metals consequently lead to a high specific capacitance.
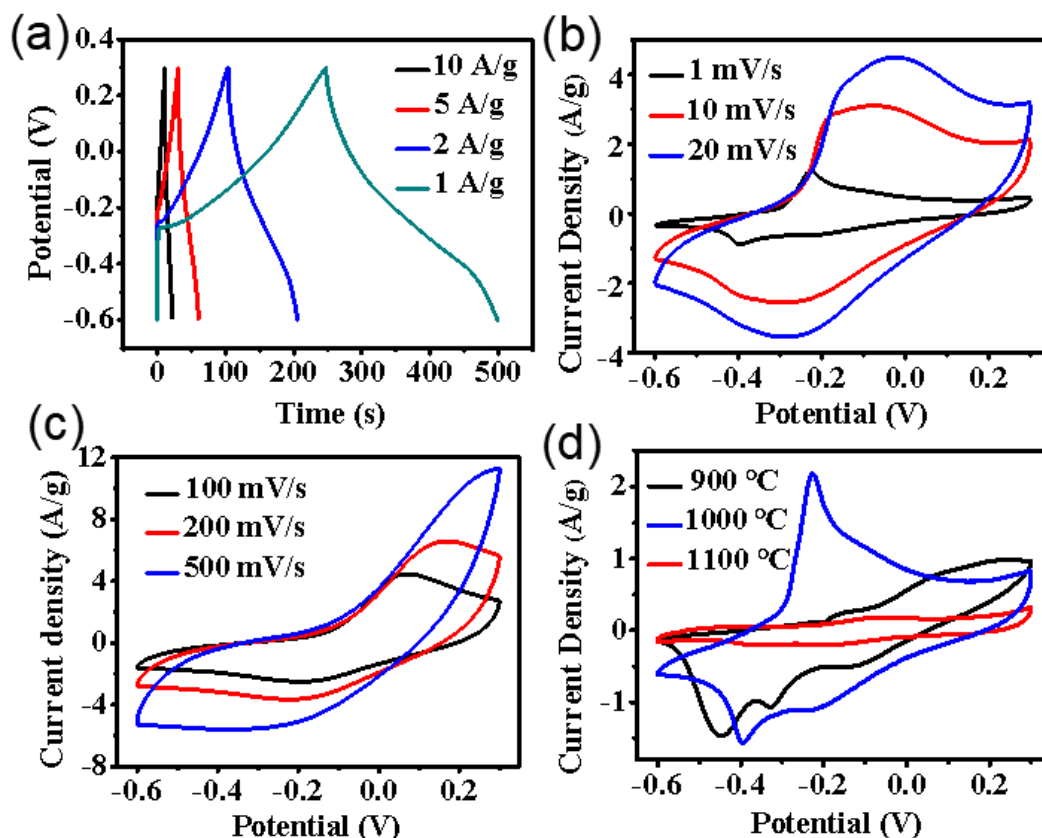
Figure 7. (a) Galvanostatic charging/discharging curves of the MnPNC at different current densities, (b) and (c) CV curves of the MnPNC at various scan rates, (d) CV curves of the MnPNC after treatment at different temperatures at 1 mV/s.

However, much excessive use of MnO_2 will significantly deteriorate the retention rate due to the dissolution of transition metal in electrolytes. Especially for the retention rate, the low mass loading of MnO_2 will appeal to a relatively high retention rate while the excessive use of MnO_2 will result in a poor retention rate. In our study, a theoretical ~5 wt% mass loading of MnO_2 gives rise to a moderate capacitance but an extraordinary cycling stability of 15000 cycles with a capacitance retention maintained 100 %, indicating the protecting carbon layer indeed functions as an armor to inhibit the dissolution of transition metals as well as offers an improved charge transfer route.

Importantly, It seems that the mass loading of MnO_2 shows no correlation with the cycling stability. Either high or low loading of active materials would possibly lead to a loss of charging/discharging cycles [33-52]. Therefore, a well-designed protecting layer with fine microstructure and morphology would markedly increase the conductivity and cycling stability. Our work is a typical case demonstrating that a low mass loading of active material is capable of pursing the high cycling stability via the introduction of delicate carbon protecting layer.

Table 1. Comparison of electrochemical performance of carbon/MnO_2 based supercapacitors.

Carbon/MnO_2 composites	Cs (F/g)	Measurement Condition	Electrolyte	Cycles	Capacitance retention (%)	Ref.
MnO_2/N-RGO	275.2	2 mA/cm^2	1 M Na_2SO_4	1000	98.3	33
MnO_2 -NW@Graphite	380.4	1 A/g	1 M KOH	2000	80	34
MnO_2/NRGO	522	2 mV/s	0.5 M Na_2SO_4	4000	96.3	35
NG-MnO_2	220	0.5 A/g	1 M Na_2SO_4	1000	98.3	36
N doped ACF core/MnO_2	26.64 mF/cm^2	0.1 mA/cm^2	1 M Na_2SO_4	8000	96	37
NCNTs@MnO_2	219	1 A/g	0.5 M Na_2SO_4	1000	86.8	38
MnO_2/HPC	87.7	3 mA/cm^2	1 M Na_2SO_4	1000	97.6	39
MnO_2/BPC	139.6	0.3 A/g	1 M Na_2SO_4	1000	92.3	40
CMMO	344	1 A/g	2 M KOH	5000	75	41
MnO_2/PEDOT	89.7 mF/cm^2	10 mV/s	1 M KCl	5000	97.1	42
MnO_2/porous carbon	459	1 A/g	6 M KOH	1000	90	43
MnO_2@C-110	655.31	1 A/g	6 M KOH	5000	87.2	44
MnO_2/HCS-30	255	1 A/g	1 M Na_2SO_4	5000	93.9	45
AC/MnO_2	134	0.5 A/g	1 M Na_2SO_4	10000	125	46
CNT@NCT@MnO_2	210	0.5 A/g	Na_2SO_4/PVA gel	1000	90.28	47
CNT-MnO_2	77.83	0.689 A/g	PVA/LiCL gel	8000	91.8	48
Nano-wrinkle MnO_2	327.4	0.1 A/g	1 M Na_2SO_4	7500	70	49
Al-doped MnO_2	101	200 mV/s	1 M Na_2SO_4	20000	99.6	50
PEDOT:PSS/MnO_2	87.4	5 mV/s	0.5 M Na_2SO_4	—	—	51
MnO_2/N-C	340.1	1 A/g	1 M KOH	3000	87.6	52
MnPNC	341	1 A/g	6 M KOH	15000	100	This work

4. CONCLUSION

In summary, biomass egg yolk has been used to prepare a hierarchically porous carbon as a protecting layer for MnO_2 nanosheets, in which the carbon is enriched with P, N, O dopants. The as-

obtained MnPNC exhibited a specific capacitance of 341 F/g at a current density of 1 A/g in 6 M KOH, with no specific capacitance loss even after 15000 cycles. Such a remarkable strategy for the synthesis biomass-derived transition metal-based supercapacitors will pave an alternative avenue in exploring novel hybrid materials for supercapacitors with outstanding electrochemical performance.

References

1. H. Jiang, D. Y. Ren, H. F. Wang, Y. J. Hu, S. J. Guo, H. Y. Yuan, P. J. Hu, L. Zhang, C. Z. Li, *Adv. Mater.*, 27 (2015) 3687–3695.
2. L. Miao, H. Duan, M. X. Liu, W. J. Lu, D. Z. Zhu, T. Chen, L. C. Li, L. H. Gan, *Chem. Eng. J.*, 317 (2017) 651–659.
3. J. Deng, M. M. Li, Y. Wang, *Green Chem.*, 18 (2016) 4824–4854.
4. X. H. Lu, M. H. Yu, G. M. Wang, Y. X. Tong, Y. Li, *Energy Environ. Sci.*, 7 (2014) 2160–2181.
5. C. Jia, T. Li, C. J. Chen, J. Q. Dai, I. M. Kierzewski, J. W. Song, Y. J. Li, C. P. Yang, C. W. Wang, L. B. Hu, *Nano Energy*, 36 (2017) 366–373.
6. D. M. Kang, Q. L. Liu, J. J. Gu, Y. S. Su, W. Zhang, D. Zhang, *ACS Nano*, 9 (2015) 11225–11233.
7. Z. S. Iro, C. Subramani, S. S. Dash, *Int. J. Electrochem. Sci.*, 11 (2016) 10628–10643.
8. C. Liu, X. Yan, F. Hu, G. Gao, G. Wu, X. Yang, *Adv. Mater.*, 30 (2018) 1705713.
9. V. Ruiz, S. Roldan, I. Villar, C. Blanco, R. Santamaria, *Electrochim. Acta.*, 95 (2013) 225–229.
10. D. W. Wang, F. Li, Z. S. Wu, W. Ren, H. M. Cheng, *Electrochem. Commun.*, 11 (2009) 1729–1732.
11. C. G. Liu, Z. N. Yu, D. Neff, A. Zhamu, B. Z. Jang, *Nano Lett.*, 10 (2010) 4863–4868.
12. C. Zhang, W. Lv, Y. Tao, Q. H. Yang, *Energy Environ. Sci.*, 8 (2015) 1390–1403.
13. S. Chen, W. Xing, J. Duan, X. Hu, S. Z. Qiao, *J. Mater. Chem. A*, 1 (2013) 2941–2954.
14. L. L. Zhang, X. S. Zhao, *Chem. Soc. Rev.*, 38 (2009) 2520-2531.
15. G. Wang, L. Zhang, J. Zhang, *Chem. Soc. Rev.*, 41 (2012) 797e828.
16. M. Huang, F. Li, F. Dong, Y. X. Zhang, L. L. Zhang, *J. Mater. Chem. A*, 3 (2015) 21380–21423.
17. S.W. Lee, J. Kim, S. Chen, P.T. Hammond, Y. Shao-Horn, *ACS Nano*, 4 (2010) 3889–3896.
18. C. Y. Wan, H. Y. Shen, X. R. Ye, F. H. Wu, *Int. J. Electrochem. Sci.*, 13 (2018) 12320–12330.
19. H. U. Shah, F. P. Wang, M. S. Javed, R. Saleem, M. S. Nazir, J. B. Zhan, Z. U. H. Khan, M. U. Farooq, S. Ali, *Int. J. Electrochem. Sci.*, 13 (2018) 6426–6435.
20. Y. L. Li, L. H. Li, G. W. Chu, X. F. Zeng, J. F. Chen, L. Shao, *Int. J. Electrochem. Sci.*, 11 (2016) 9644–9655.
21. L. Deng, G. Zhu, J. Wang, L. Kang, Z. H. Liu, Z. Yang, Z. Wang, *J. Power Sources*, 196 (2011) 10782–10787.
22. Z. S. Wu, W. Ren, D. W. Wang, F. Li, B. Liu, H. M. Cheng, *ACS Nano*, 4 (2010) 5835–5842.
23. L. Chen, Y. Z. Zuo, Y. Zhang, Y. M. Gao, *Int. J. Electrochem. Sci.*, 13 (2018) 642–654.
24. E. Miniach, A. Sliwak, A. Moyseowicz, L. F. Garcia, Z. Gonzalez, M. Granda, R. Menendez, G. Gryglewicz, *Electrochim. Acta*, 240 (2017) 53–62.

25. W. Kong, L. Yan, Y. Luo, D. Wang, K. Jiang, Q. Li, S. Fan, J. Wang, *Adv. Funct. Mater.*, 27 (2017) 1606663.
26. H. Z. Naderi, M. R. Ganjali, P. Norouzi, *Int. J. Electrochem. Sci.*, 11 (2016) 4267–4282.
27. H. Huang, W. Zhang, Y. Fu, X. Wang, *Electrochim. Acta*, 152 (2015) 480–488.
28. W. Wei, X. Cui, W. Chen, D. G. Ivey, *Chem. Soc. Rev.*, 40 (2011) 1697–1721.
29. X. M. Dong, H. L. Jin, R. Y. Wang, J. J. Zhang, X. Feng, C. Z. Yan, S. Q. Chen, S. Wang, J. Wang, J. Lu, *Adv. Energy Mater.*, 8 (2018) 1702695.
30. J. J. Zhang, H. P. Zhao, J. Li, H. L. Jin, X. C. Yu, Y. Lei, S. Wang, *Adv. Energy Mater.*, 9 (2019) 1803221.
31. H. L. Jin, J. Li, Y. F. Yuan, J. Wang, J. Lu, S. Wang, *Adv. Energy Mater.*, 8 (2018) 1801007.
32. H. L. Jin, X. Feng, J. Li, M. Li, Y. Z. Xia, Y. F. Yuan, C. Yang, B. Dai, Z. Q. Lin, J. Wang, J. Lu, S. Wang, *Angew. Chem. Int. Ed.*, 58 (2019) 2397–2401.
33. J. Mei, L. Zhang, *Electrochimica Acta*, 173 (2015) 338–344.
34. Y. Bi, A. Nautiyal, H. Zhang, H. Yan, J. Luo, X. Zhang, *Ceramics Int.*, 44 (2018) 5402–5410.
35. H. R. Naderi, P. Norouzi, M. R. Ganjali, *Appl. Surf. Sci.*, 366 (2016) 552–560.
36. J. Dong, G. Lu, F. Wu, C. Xu, X. Kang, Z. Cheng, *Appl. Surf. Sci.*, 427 (2018) 986–993.
37. S. Jiang, S. Cheng, Y. Huang, T. Shi, Z. Tang, *Ceramics Int.*, 43 (2017) 7916–7921.
38. X. Ou, Q. Li, D. Xu, J. Guo, F. Yan, *Chem. Asian J.*, 13 (2018) 545–551.
39. X. Li, Z. Wang, L. Guo, D. Han, B. Li, Z. Gong, *Electrochimica Acta*, 265 (2018) 71–77.
40. G. Yang, S. J. Park, *J. Alloys Comp.*, 741 (2018), 360–367.
41. Y. Wang, A. Fu, X. Liu, Y. Wang, Y. Li, P. Guo, H. Li, X. S. Zhao, *J. Alloys Comp.*, 717 (2017) 341–349.
42. H. Zhou, X. Zhi, H. J. Zhai, *Mater. Electron.*, 29 (2018) 3935–3942.
43. M. Liu, L. Gan, W. Xiong, Z. Xu, D. Zhu, L. Chen, *J. Mater. Chem. A*, 2 (2014) 2555–2562.
44. Y. Xie, C. Yang, P. Chen, D. W. Yuan, K. K. Guo, *J. Power Sources*, 425 (2019) 1–9.
45. W. Du, X. N. Wang, J. Zhan, X. Q. Sun, L. T. Kang, F. Y. Jiang, X. Y. Zhang, Q. Shao, M. Y. Dong, H. Liu, V. Murugadoss, Z. H. Guo, *Electrochim. Acta*, 296 (2019) 907–915.
46. A. J. Paleo, P. Staiti, A. Brigandi, F. N. Ferreira, A. M. Rocha, F. Lufrano, *Energy Storage Mater.*, 12 (2018) 204–215.
47. Y. H. Wang, D. Y. Zhang, Y. Lu, W. X. Wang, T. Peng, Y. G. Zhang, Y. Guo, Y. G. Wang, K. F. Huo, J. K. Kim, Y. S. Luo, *Carbon*, 143 (2019) 335–342.
48. Q. F. Wang, Y. Ma, X. Liang, D. H. Zhang, M. H. Miao, *Chem. Eng. J.*, 371 (2019) 145–153.
49. W. Yan, K. Zhuo, J. L. Ji, Q. Zhang, S. B. Sang, *Int. J. Electrochem. Sci.*, 14 (2019) 4496–4507.
50. Y. H. Zeng, Y. Cong, T. T. Jiang, C. X. Zhang, Y. X. Gao, H. Q. Shi, Y. M. Dai, *Int. J. Electrochem. Sci.*, 14 (2019) 4350–4360.
51. X. J. Li, C. Zhou, L. L. Shen, W. Q. Zhou, J. K. Xu, C. Luo, J. Hou, R. R. Tan, F. X. Jiang, *Int. J. Electrochem. Sci.*, 14 (2019) 4632–4642.
52. X. X. Du, Q. Chen, C. L. Xiang, Y. J. Zou, F. Xu, J. J. Xie, L. X. Sun, *Int. J. Electrochem. Sci.*, 14 (2019) 4195–4205.